THE COMBINED USE OF MICRO-CT IMAGING, IN-SITU LOADING AND NON-RIGID IMAGE REGISTRATION FOR 3D EXPERIMENTAL LOCAL STRAIN MAPPING ON POROUS BONE TISSUE ENGINEERING SCAFFOLDS UNDER COMPRESSIVE LOADING

Greet KERCKHOFS[1,2], Grzegorz PYKA[1,2], Dirk LOECKX[3,4], Simon VAN BAEL[2,5], Jan SCHROOTEN[1,2] and Martine WEVERS[1]

[1] Department of Metallurgy and Materials Engineering, Katholieke Universiteit Leuven, B-3001 Leuven, Belgium
[2] Prometheus, Division of Skeletal Tissue Engineering, Katholieke Universiteit Leuven, B-3000 Leuven, Belgium
[3] Department of Electrical Engineering, Division ESAT - PSI, Centre for the Processing of Speech & Images, Katholieke Universiteit Leuven, B-3001 Leuven, Belgium
[4] Medical imaging centre, U.Z. Leuven, B-3000 Leuven, Belgium
[5] Department of Mechanical Engineering, Division of Production engineering, Machine design and Automation, Katholieke Universiteit Leuven, B-3001 Leuven, Belgium

ABSTRACT

Porous structures are used in many industrial applications such as thermal insulation, packaging and filters, food and beverage, pharmaceuticals, but also in biomedical applications such as scaffolds for bone tissue engineering (TE). To understand, simulate and eventually predict the behaviour of porous structures during loading in order to assess their functionality, a thorough knowledge of the relationship between their morphology and mechanical behaviour is needed. Also, and specifically for bone TE scaffolds, calculating or predicting the local strains under mechanical loading can be useful to analyze strain-dependent cell behaviour on the surfaces of the porous scaffolds. This research analyzed rapid prototyped (RP) porous Ti6Al4V structures, to be used as bone TE scaffold, by correlating structural characteristics (meso- and microscale morphology) with mechanical performance (stiffness, strain distribution and failure) using quantified 3D, multimodular characterization techniques. This analysis enables design optimization and RP production feedback in function of the envisioned requirements. Because it is known that, apart from the strains present on the surfaces of the scaffold, also the surface topology has a significant influence on the cell behaviour, the effect of surface modification of the porous Ti6Al4V scaffolds on their local strain distribution and mechanical behaviour has been assessed.

1. INTRODUCTION

Instead of standard treatments for large bone traumas, which focus on bone reconstruction, bone tissue engineering (TE) emphasizes on tissue regeneration. TE applies a combination of an open porous structure, also called bone TE scaffold, with osteogenic cells that, after a process of cell seeding and bioreactor culture, can be implanted in the large bone defect[1-3]. Several production techniques can be used to fabricate bone TE scaffolds. Traditional methods include solvent-casting and particulate-leaching, gas foaming, fibre meshes/fibre bonding, phase separation, melt moulding, emulsion freeze drying, solution casting and freeze drying[4]. These methods, however, have largely been unsuccessful in controlling the internal architecture to a high degree of accuracy or homogeneity. Since previous research[5, 6] has demonstrated that control over the interior architecture is crucial to ensure TE scaffold vascularisation and bone deposition and because creation of TE scaffolds with identical internal architectures is essential for mass transfer and mechanobiology, an evolution from random porous TE scaffolds to porous TE scaffolds that are based on a robust computer design is noticed[7, 8]. Regular architecture TE scaffolds permit cells to be seeded in the core much more readily than random architecture scaffolds and create environments which encourage uniform conditions for promoting cell viability and functional behaviour. The added advantage of developing regular architecture scaffolds is that they permit parametric analyzes to be conducted, which is essential in scientific investigations of how scaffolds perform as a function of their physical characteristics.

For the design and production of bone TE scaffolds with a high morphological property control, rapid prototyping (RP) techniques offer a solution[4, 5, 9-15]. Although RP techniques allow a high morphological control at the meso-scale, metal structures produced by selective laser melting (SLM) for example are known to have variability in morphological (micro-scale) and mechanical properties due to local inhomogeneities in surface roughness and internal stresses. Thus, next to achieving predefined properties, obtaining these properties at a reproducible level is also a key issue, as it is well understood that small/local changes in the porous structure's morphology may cause significant changes in the apparent properties. Also, primary interaction between the TE scaffolds and the surrounding biological environment depends strongly on the surface properties of the TE scaffold. It was shown recently that the surface topography has a strong influence on osteoblast differentiation and mineralization[16-23]. For this reason, it is essential to find the correct surface modification and optimization for the future design and production of TE scaffolds. Additionally, as proliferation and differentiation of the osteogenic cells are amongst others also promoted by mechanical strains caused by the deformation of the structures to which the cells attach [24], the local strain distribution on the surfaces of the TE scaffolds on which the cells are seeded can influence cell behaviour and thus also subsequent bone formation. To reduce the variability due to local inhomogeneities in surface roughness and to be able to fine-tune the surface topology in a controlled manner, this study has applied surface modification by chemical and electrochemical etching. This allows controlling and optimizing the morphological properties of the TE scaffolds at the microscale, and thus also the global and local mechanical behaviour, and correlating cell behaviour with (i) surface roughness and (ii) surface strains.

For the experimental quantification of the surface roughness and the local strains during compressive loading, the combination of micro-CT imaging, 3D image analysis and in-situ loading, including local strain mapping of the micro-CT scans at different loading steps, has been used. To accomplish the local strain mapping, digital volume correlation (DVC) of micro-CT scans at different loading steps could be applied as first reported in Ref.[25]. Current DVC techniques [26-28], however, suffer from limiting assumptions regarding the nature of the relationship between corresponding voxel intensities of both the images before and after loading, and from the need for regularization or smoothing of the deformation field in order to suppress errors and noise in the estimated deformations. A novel and more robust technique based on automated multimodality non-rigid intensity-based image registration [29-31] has provided a solution, since it eliminates the limitations of current DVC approaches. The resulting strain maps have been used to quantify the local strains on the surface of the TE scaffolds prior to and after surface modification, and thus to assess the influence of the surface roughness on the local mechanical properties, and to predict the material failure modes under compressive loading.

The purpose of this study was two-fold: (i) to quantify experimentally the local strain distribution and failure modes in porous structures using a novel strain mapping tool based on non-rigid image registration and (ii) to compare these results for the 'as produced' and 'surface modified' porous scaffolds with regard to mechanical behaviour and failure. Therefore, porous Ti6Al4V structures produced by selective laser melting (SLM) [15], a RP technique, were used.

2.   MATERIALS AND METHODS

2.1. Design and production of the porous Ti6Al4V structures

Cylindrical porous Ti6Al4V structures with a regular architecture were made using SLM, a relatively young RP technique. The designed pore and strut size were 1.0 mm and 0.1 mm respectively. Figure 1A shows a typical longitudinal 2D image of the Computer Aided Design (CAD) model of the design. The design was based on a parametric unit cell (fig. 1B and 1C), which consisted entirely of identical beams with a constant circular cross-section.
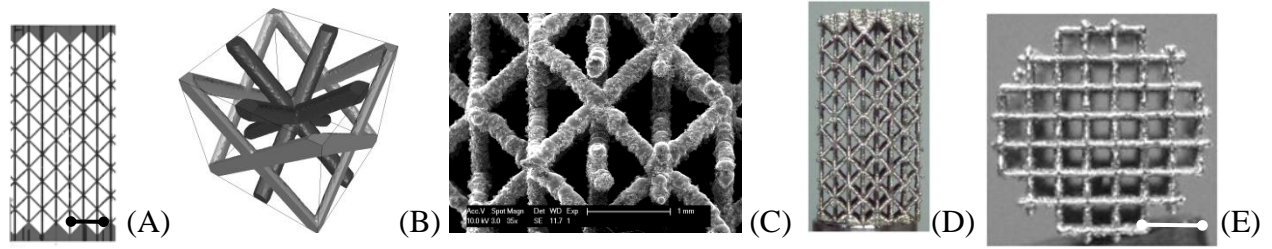
Figure 1. Examples of the Ti6Al4V porous scaffolds: A) a CAD design, B) the parametric unit cell, C) a SEM picture of the unit cell, D) a typical digital image of the side view of a Ti6Al4V porous scaffold and D) the top view of a typical Ti6Al4V porous scaffold. Scale bars = 2 mm.

The designed structures were produced on an in-house developed SLM machine using Ti6Al4V powder [CL40TI – Concept laser GmbH – Lichtenfels, Germany]. Fig. 1D and 1E visualize a produced porous Ti6Al4V structure respectively from the side and top view. Table 1 gives an overview of the powder and SLM machine specifications, and the SLM process parameters. Magics 3D [Materialise NV – Haasrode, Belgium] was applied to generate the CAD-file. All SLM produced structures had a mean radius of 3.02 ± 0.05 mm and a mean height of 11.72 ± 0.20 mm. The designed beam thickness was chosen below the dimensions of the SLM melt pool (0.18 mm) to define the minimum SLM feature size. Hence, a larger effective beam thickness and a smaller effective pore size were expected for the SLM produced structures.

Table 1: Specifications of the Ti6Al4V powder, characteristics of the SLM machine and the SLM process parameters.

Specification of the Ti6Al4V powder		Characteristics SLM machine and SLM process parameters	
Density:	4.42 g/cm³	*Laser type:*	Yb:YAG fibre laser
Max. Tensile Strength:	1000 MPa	*Laser spot size:*	80 µm
Tensile Strength at 0.2% deformation:	920 MPa	*Maximum laser power:*	300 W
Max. Strain:	12%	*Laser power during production:*	39 W
E-modulus:	110 GPa	*Scanning speed:*	260 mm/s
Melting point:	1649°C	*Powder layer thickness:*	30 µm
Average Grain Size:	25-45 µm		

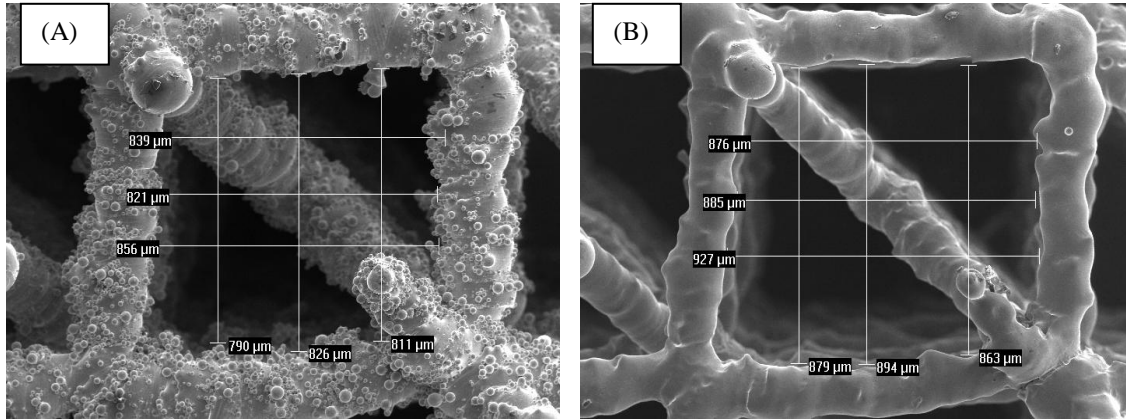## 2.2. Surface modification of the porous Ti6Al4V structures

Figure 2. Typical SEM image of an (A) 'as produced' and (B) 'surface modified' porous Ti6Al4V scaffold. For the 'as produced' sample, the non-melted powder grains attached to the strut surface are clearly visible.

The Ti6Al4V scaffolds after production reveal a large and highly inhomogeneous roughness caused by non–melted powder grains attached to the strut surface (fig. 2A). An appropriate surface roughness reduction procedure was developed, which apart from removing the inhomogeneities of the struts, allows to obtain a cell-friendly strut topology with smooth surface or, dependent on the applied surface treatment and preference of the cells, with a 'nanopits-like' morphology. First, the 'as produced' samples were polished chemically in order to remove the attached non-melted powder grains and in a

second step, electrochemical polishing was applied to obtain the desired surface morphology. Scanning electron microscopy (SEM) images of 'as produced' and 'surface modified' struts are shown in figure 2A and 2B respectively.

During chemical polishing, the samples were immersed in a chemical solution containing hydrofluoric acid and water. This procedure allowed removing all the attached powder grains on the scaffold surface. As a second step, smoothening of the strut surface has been performed by electrochemical polishing. The experimental setup is shown in figure 3, where the sample (anode, +), placed in the middle of the cylindrical platinum basket (cathode, –) (Ø 30mm, 40mm height), was suspended with a platinum wire (Ø 300µm) in a polyethylene beaker filled with electrolyte. The anode and the cathode were connected with cables to the direct current source (TS3021S –30V/2A, Thurlby Thandar Instruments Ltd., UK). The electrolyte was stirred during polishing with a magnetic stirrer. The combination of

Figure 3. The experimental setup built for the electrochemical polishing of the Ti6Al4V scaffolds

chemical and electrochemical polishing gives an opportunity to modify the strut surface in a controlled way, allowing to obtain smooth surfaces (fig. 4A) as well as 'nanopits-like' surfaces (fig. 4B).
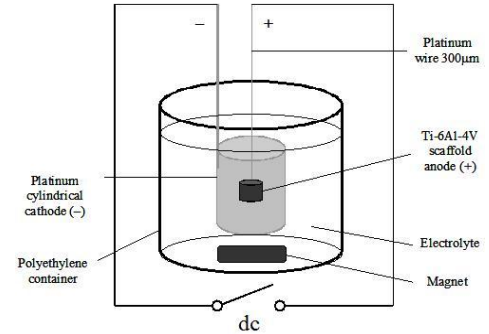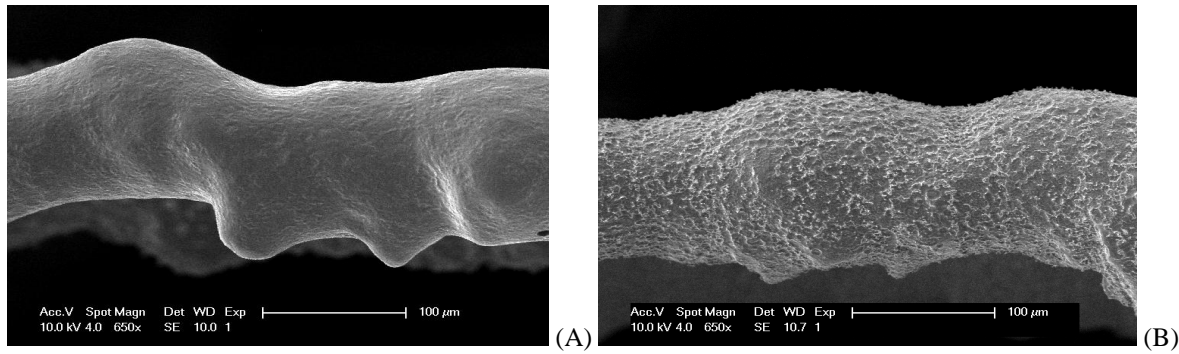

Figure 4. Typical SEM images of a single strut of a Ti6Al4V porous scaffold after chemical and electrochemical etching, showing: (A) a smooth surface and (B) a 'nanopits-like' surface.

2.3. Micro-CT imaging, in-situ mechanical loading and 3D image analysis

For micro-CT imaging of the porous structures, a Philips HOMX 161 X-ray system with AEA Tomohawk CT software was used. Characteristics of the device and the applied acquisition parameters can be found in Ref. [32]. The micro-CT system was equipped with an in-house developed mechanical loading stage installed in the micro-CT device. For the in-situ mechanical measurements on the Ti6Al4V structures, a compression rate of 0.20 mm/min was applied, using a load cell of 3 kN. Prior to loading, the morphology of the 'as produced' and 'surface modified' porous Ti6Al4V structures was quantified by 3D image analysis of the micro-CT images. Therefore, the images were first binarized based on physical measurements of the volume fraction of the samples (Archimedes principle). An extended set of morphological parameters was then determined using commercially available image analysis software, named CTAn [SkyScan NV – Kontich, Belgium]. The pore size and beam thickness distributions were obtained by the model-independent technique from Hildebrand and Rüegsegger [33] from the binarized micro-CT images.

2.4. Local strain mapping

While correlation-based image registration assumes a linear relationship between the micro-CT intensities of corresponding points inside the structures in different scans [26], this assumption is not made in maximization of mutual information (MMI) since it is based on a statistical measure of intensity similarity. Therefore MMI provides a more general and robust registration criterion [34].

Instead of using a block-matching scheme followed by post-processing for regularization, the regularization is directly included in the deformation model itself by applying a 3D B-spline function, which is intrinsically smooth at local scales and may be regularized at larger scales if needed by including additional penalty terms that constrain the local rigidity of the material [35]. The B-spline is constructed as a continuous and derivable combination of piecewise second degree polynomials over a lattice with, in this study, a final resolution of 16x16x16 voxels. The local strains in each point of interest as then computed at any arbitrary point by analytic differentiation of the deformation field, without the need for prior segmentation or post smoothing. The micro-CT datasets at different loading steps were used as input for the non-rigid image registration tool. Analysis of the local strain maps allowed locating where the most critical strains occur and enabled quantification of the strain distribution for different applied mechanical loads. In this way, the difference in micro-scale mechanical behaviour between the 'as produced' and the 'surface modified' structures was assessed. Additionally, the observation and prediction of the failure modes of the porous structures was possible.

3. RESULTS AND DISCUSSION

3.1. Morphological and global mechanical characterization of the porous Ti6Al4V structures prior to and after surface modification

Table 2. Micro-CT image analysis-based morphological characterization of the porous Ti6Al4V scaffolds prior to and after surface modification.

	Sample volume [mm³]	Porosity [%]	Avg. strut thickness [μm]
'As produced'	57.47 ± 1.31	86.31 ± 0.16	213.81 ± 0.57
'Surface modified'	33.40 ± 2.19	92.03 ± 0.74	169.05 ± 7.58

The morphology of the porous Ti6Al4V structures prior to and after surface modification was characterized both on the meso- and micro-scale. The micro-CT based meso-scale characteristics, shown in table 2, indicated a significant decrease in the strut thickness and sample volume after surface modification, while the porosity increased. The micro-scale morphology, and more specific the surface roughness, was measured based on the profile lines in high-resolution SEM images of single struts. The results (figure 5) show that the roughness decreased after surface modification, but also a difference in surface roughness between the bottom and the top of the struts was noticed, caused by gravity on the non-melted powder grains.
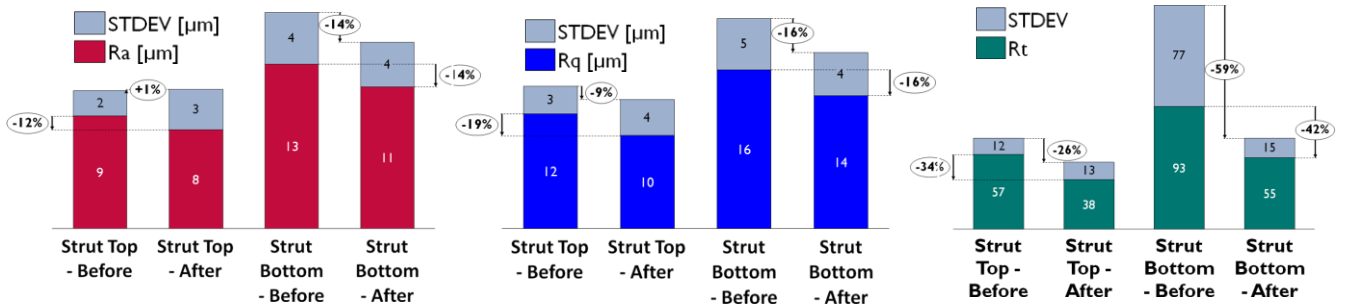

Figure 5. Roughness parameters (R_a, R_q and R_t) of the Ti6Al4V scaffolds prior to and after surface modification.

Continuous compression tests were performed on the 'as produced' and 'surface modified' porous structures. The stiffness, strength and strain at maximum load were calculated (table 3), showing a significant decrease in the mechanical properties after surface modification, mostly because of the reduction in the strut thickness.

Table 3. Mechanical properties of the porous Ti6Al4V scaffolds prior to and after surface modification.

	Stiffness [MPa]	Strength [MPa]	Strain at max strength [%]
'As produced'	397.07 ± 29.95	13.00 ± 0.62	6.04 ± 0.32
'Surface modified'	226.15 ± 22.45	7.41 ± 0.88	7.02 ± 0.24

3.2. Experimental quantification of local strains in relation to the surface modification

Figures 6A and 6B show a typical coronal, sagital and axial strain map (in the Z-direction) at 6.7 % of applied strain of the 'as produced' and 'surface modified' porous Ti6Al4V structures. Despite of the regularity of the designed morphology of the porous Ti6Al4V structures, figure 6A shows a rather inhomogeneous strain distribution, where a homogeneous distribution was expected (except near the boundaries). This inhomogeneity resulted from the boundary conditions related to the mechanical measurements (causing also barrelling), and from irregularities in the morphology of the produced Ti6Al4V structures. For example, figure 7A and 7B show high magnification SEM images of a porous Ti6Al4V structure. In figure 7A, the arrow indicates a strut that appears not to be straight near the nodes. Figure 7B shows the variability in strut thickness on a micron-scale and a significant thinning of the strut close to the node. Both the irregularity in shape and the variability in strut thickness influence the local strain concentrations significantly. The dimensions of the non-melted powder grains on the strut surfaces of the 'as produced' porous Ti6Al4V structures are in the same range as the spatial resolution of the micro-CT images, and hence might not be accounted for individually, but will also have an influence of the local strain concentrations.
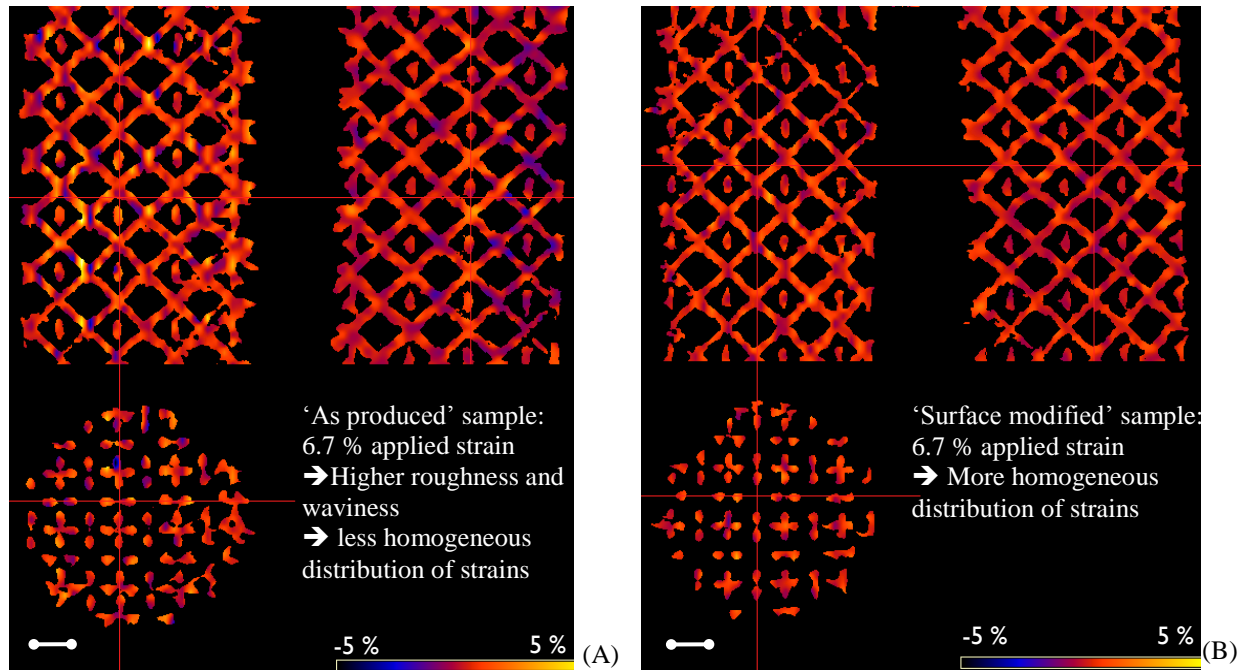

Figure 6. Typical strain maps (coronal, sagital and axial) of the obtained 3D µCT images of an (A) 'as produced' and (B) 'surface modified' compressed porous Ti6Al4V structure. Scale bars = 1 mm.
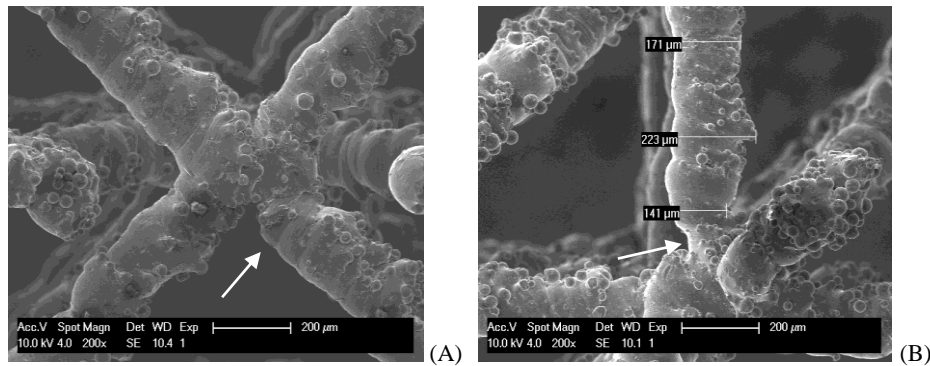

Figure 7: Typical SEM images near the nodes of a porous Ti6Al4V structure indicating (A) that struts can form bends near the node and (B) that there is a significant thinning of the strut close to the node and a large variability in strut thickness.

Indeed, after surface modification (fig. 6B), a more homogeneous and smaller distribution of the strain was found, which was confirmed in figure 8 where the strain distribution at 1.7 % and 6.7 % of applied load is shown both for the 'as produced' and 'surface modified' structures. Surface modification thus allows homogenization and a better control of the surface strains. Also, because the strut thickness decreased, smaller strains were expected since the surface strain is directly proportional to distance from the midsection of the strut to the surface (~ strut thickness). This was confirmed in figure 8.
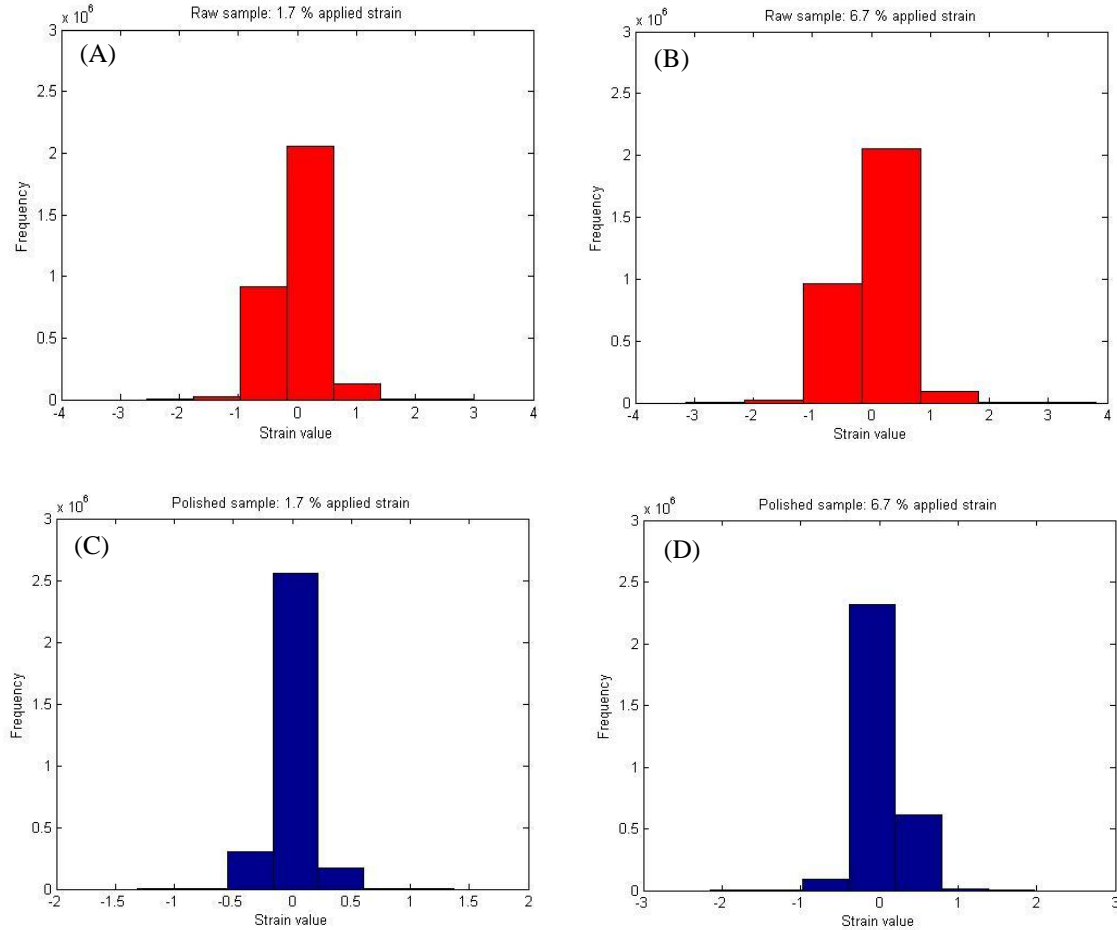

Figure 8: The strain distribution curves for an 'as produced' porous Ti6Al4V sample loaded until (A) 1.7 % and (B) 6.7 % of applied strain and the strain distribution curves for a 'surface modified' porous Ti6Al4V sample loaded until (C) 1.7 % and (D) 6.7 % of applied strain.

3.3. Experimental quantification of local strains in relation to the failure modes of the porous Ti6Al4V structures prior to and after surface modification

3.3.1. Failure behaviour of the porous Ti6Al4V structures prior to and after surface modification at meso-scale

Both for the 'as produced' and 'surface modified' porous Ti6Al4V structures, because of the frictionless clamping of the samples and the rather high Poisson's ratio, barrelling of the structures was noticed as can be seen in the digital images of a loaded sample (fig. 9A). Failure occurred in the midsection of the samples rather than at the top or bottom (fig. 9A, 9B and 9C). Indeed, the largest strain values were found in the middle of the sample (fig. 6). The meso-scale failure behaviour of the 'as produced' and 'surface modified' porous Ti6Al4V structures is similar, although the 'surface modified' samples fail at a larger applied strain (fig. 9B and 9C).
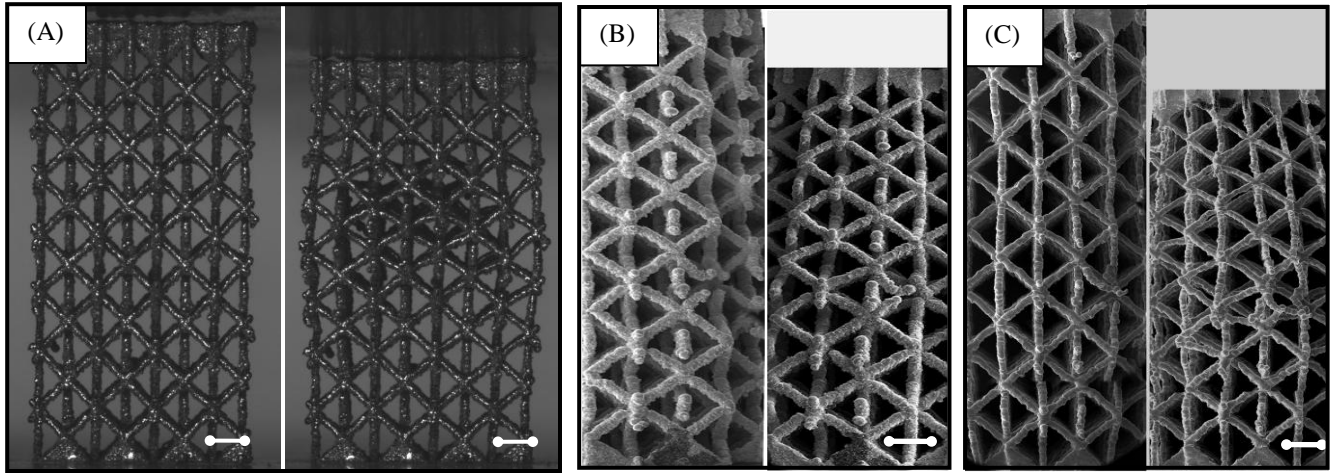
Figure 9. (A) Typical digital images of an 'as produced' porous Ti6Al4V structure prior to (left) and after (right) loading until final failure, and typical SEM images of the porous Ti6Al4V samples prior to (left) and after (right) loading until final failure (B) prior to surface modification and (C) after surface modification. Scale bars = 1 mm.

3.3.2. Failure behaviour of the porous Ti6Al4V structures prior to and after surface modification at micro-scale

Figure 10 shows a magnification of a representative longitudinal 2D strain map of an 'as produced' porous Ti6Al4V structure (fig. 6A) in the z-direction at 6.7 % of applied strain. The latter indicates that the largest strain concentrations occurred near the nodes (zone 1) and that they were compressive. Away from the nodes smaller strains were noticed. In the midsection of the beams either tensile strains (zone 2) or high compressive strains (zone 3) were found, which indicated buckling of the beams. Identical behaviour is noticed for the 'surface modified' structures. Based on the strain mapping one would predict fracture near the nodes. These findings are directly linked to aforementioned morphological irregularities near the nodes (fig. 7A and 7B), and are substantiated by typical SEM images prior to and after compression (fig. 10B and 10C respectively) of an 'as produced' porous Ti6Al4V structure. Indeed, where the struts appear not to be straight near the nodes or where the struts show a significant thinning, as in fig. 10B and 10C, failure occurs.
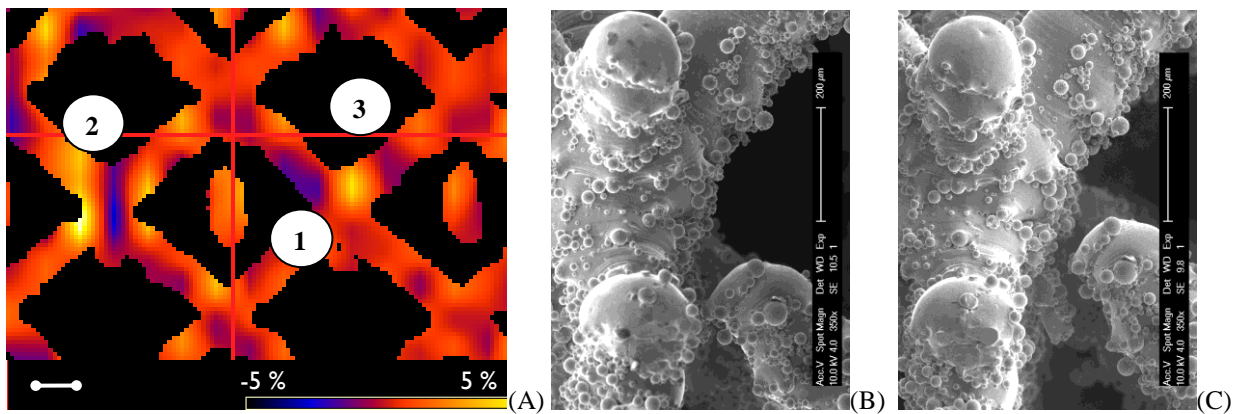

Figure 10: (A) A magnification of the representative longitudinal 2D strain map in the z-direction of fig. 6A at 6.7 % of applied strain. The largest strain concentrations occurred near the nodes (zone 1) and that they were compressive. In the midsection of the beams either tensile strains (zone 2) or high compressive strains (zone 3) were found (scale bar = 250 μm), and a high magnification SEM image of a typical node (B) prior to and (C) after compression.

4. CONCLUSIONS

The combination of micro-CT imaging and 3D image analysis with in-situ mechanical loading allowed local strain mapping based on non-rigid image registration by MMI. This multimodular, 3D characterization approach is a valuable tool (i) for experimental quantification of the local strain

distribution and failure modes in porous structures and (ii) to evaluate the effect of surface modification on the mechanical behaviour. What is more, the combination allowed investigating the failure behaviour of the porous, SLM produced, Ti6Al4V TE scaffolds both at meso- and micro-scale. The experimental quantification of the local strains will also assist in a robust and systematic design of TE scaffolds with regard to the local surface strain distribution to promote the proliferation and differentiation of cells. Surface modification showed to be useful for homogenization and control of both the surface topology and the local mechanical properties. In order to correlate the cell behaviour to the experimentally determined local surface strains, in future experiments the osteogenic capacity of different cell-seeded TE scaffolds will be assessed in a mechanically-stimulating perfusion bioreactor. Additionally, the cell behaviour depending on the surface topology will be investigated, thus allowing optimization of the design, production and surface modification of porous Ti6Al4V structures to be used as TE scaffolds based on the biological outcome.

5.   ACKNOWLEDGEMENTS

6.   REFERENCES

[1]   Bakker A. et al., Quantitative Screening of Engineered Implants in a Long Bone Defect Model in Rabbits, Tissue Engineering: Part C, 2008;14 (3):251-260.
[2]   Cancedda R. et al., A tissue engineering approach to bone repair in large animal models and in clinical practice, Biomaterials, 2007;28 (29):4240-4250.
[3]   Salgado A.J. et al., Bone tissue engineering: State of the art and future trends, Macromol. Biosci., 2004;4 (8):743-765.
[4]   Hutmacher D.W., Scaffolds in tissue engineering bone and cartilage, Biomaterials, 2000;21 (24):2529-2543.
[5]   Chu T.M.G. et al., Mechanical and in vivo performance of hydroxyapatite implants with controlled architectures, Biomaterials, 2002;23 (5):1283-1293.
[6]   Mikos A.G. et al., Prevascularization of Porous Biodegradable Polymers, Biotechnology and Bioengineering, 1993;42 (6):716-723.
[7]   Simske S.J. et al., Porous materials for bone engineering, Mater Sci Forum, 1997;250 151-182.
[8]   Snijkers F. et al., Porous Materials as Scaffold for Bone Replacement, Acers-meeting, 2005.
[9]   Bose S. et al., Processing of controlled porosity ceramic structures via fused deposition, Scripta Mater, 1999;41 (9):1009-1014.
[10]   Hollister S.J. et al., Optimal design and fabrication of scaffolds to mimic tissue properties and satisfy biological constraints, Biomaterials, 2002;23 (20):4095-4103.
[11]   Wintermantel E. et al., Tissue engineering scaffolds using superstructures, Biomaterials, 1996;17 (2):83-91.
[12]   Xiong Z. et al., Fabrication of porous poly(L-lactic acid) scaffolds for bone tissue engineering via precise extrusion, Scripta Mater, 2001;45 (7):773-779.
[13]   Leong K.F. et al., Solid freeform fabrication of three-dimensional scaffolds for engineering replacement tissues and organs, Biomaterials, 2003;24 (13):2363-2378.
[14]   Williams J.M. et al., Bone tissue engineering using polycaprolactone scaffolds fabricated via selective laser sintering, Biomaterials, 2005;26 (23):4817-4827.
[15]   Hollander D.A. et al., Structural, mechanical and in vitro characterization of individually structured Ti-6Al-4V produced by direct laser forming, Biomaterials, 2006;27 (7):955-963.

[16] Ponsonnet L. et al., Effect of surface topography and chemistry on adhesion, orientation and growth of fibroblasts on nickel-titanium substrates, Mat Sci Eng C-Bio S, 2002;21 (1-2):157-165.

[17] Ponsonnet L. et al., Relationship between surface properties (roughness, wettability) of titanium and titanium alloys and cell behaviour, Mat Sci Eng C-Bio S, 2003;23 (4):551-560.

[18] Sammons R.L. et al., Comparison of osteoblast spreading on microstructured dental implant surfaces and cell behaviour in an explant model of osseointegration, Clinical Oral Implants Research, 2005;16 (6):657-666.

[19] Wirth C. et al., Nitinol surface roughness modulates in vitro cell response: a comparison between fibroblasts and osteoblasts, Mat Sci Eng C-Bio S, 2005;25 (1):51-60.

[20] Wirth C. et al., Biomaterial surface properties modulate in vitro rat calvaria osteoblasts response: Roughness and or chemistry?, Mat Sci Eng C-Bio S, 2008;28 (5-6):990-1001.

[21] Zhao G. et al., Osteoblast-like cells are sensitive to submicron-scale surface structure, Clinical Oral Implants Research, 2006;17 (3):258-264.

[22] Masaki C. et al., Effects of implant surface microtopography on osteoblast gene expression, Clinical Oral Implants Research, 2005;16 (6):650-656.

[23] Sader M.S. et al., Effect of three distinct treatments of titanium surface on osteoblast attachment, proliferation, and differentiation, Clinical Oral Implants Research, 2005;16 (6):667-675.

[24] Ignatius A. et al., Tissue engineering of bone: effects of mechanical strain on osteoblastic cells in type I collagen matrices, Biomaterials, 2005;26 (3):311-318.

[25] Bay B.K. et al., Digital volume correlation: Three-dimensional strain mapping using X-ray tomography, Experimental Mechanics, 1999;39 (3):217-226.

[26] Verhulp E. et al., A three-dimensional digital image correlation technique for strain measurements in microstructures, J Biomech, 2004;37 (9):1313-1320.

[27] Liu L. and Morgan E.F., Accuracy and precision of digital volume correlation in quantifying displacements and strains in trabecular bone, J Biomech, 2007;40 (15):3516-3520.

[28] Zauel R. et al., Comparison of the linear finite element prediction of deformation and strain of human cancellous bone to 3D digital volume correlation measurements, Journal of Biomechanical Engineering-Transactions of the Asme, 2006;128 (1):1-6.

[29] Maintz J.B.A. and Viergever M.A., A survey of medical image registration, Medical Image Analysis, 1998;2 (1):1-36.

[30] Zitova B. and Flusser J., Image registration methods: a survey, Image and Vision Computing, 2003;21 (11):977-1000.

[31] Maes F. et al., Multimodality image registration by maximization of mutual information, Ieee Transactions on Medical Imaging, 1997;16 (2):187-198.

[32] Kerckhofs G. et al., Validation of x-ray microfocus computed tomography as an imaging tool for porous structures, Review of Scientific Instruments, 2008;79 (1):1-9.

[33] Hildebrand T. and Ruegsegger P., A new method for the model-independent assessment of thickness in three-dimensional images, J Microsc-Oxford, 1997;185 67-75.

[34] Maes F. et al., Medical image registration using mutual information, Proceedings of the Ieee, 2003;91 (10):1699-1722.

[35] Loeckx D. et al., Nonrigid image registration using free-form deformations with a local rigidity constraint, Medical Image Computing and Computer-Assisted Intervention - Miccai 2004, Pt 1, Proceedings, 2004;3216 639-646.